Research paper

Properties of one-part CaO–Na$_2$CO$_3$ activated ground granulated blast furnace slag

Qian Li[1]

Abstract: In this study, the fresh and hardened performance and durability of one-part ground granulated blast furnace slags (GGBFS) activated by solid CaO and Na$_2$CO$_3$ were discussed, and their hydration process and microstructure development were analyzed accordingly. Results showed that when the water-to-binder ratio was 0.32, the alkali-activated slag (AAS) paste exhibited lower flowability, higher yield stress and plastic viscosity. As the content of CaO and Na$_2$CO$_3$ increased, the yield stress, plastic viscosity, and compressive strength of AAS after hardening all increased. For the durability of the hardened sample, AAS with high content of activator have higher shrinkage strain and chloride ion flux. The microscopic analysis results indicated that AAS containing CaO and Na$_2$CO$_3$ exhibited more intense hydration heat release and rapid microstructure development in the early stage, thereby promoting the improvement of strength. The use of CaO and Na$_2$CO$_3$ to activate GGBFS has enormous application potential in solid waste utilization and carbon emission reduction, which can reasonably replace traditional Portland cement (PC) as a new generation of sustainable cementitious materials.

Keywords: alkali-activated slag, CaO, Na$_2$CO$_3$, performance, durability, microstructure

[1]MSc. Eng., Henan Open University, School of Architectural Engineering and Intelligent Construction, Zhengzhou 450008, China, e-mail: muzirenqing111@126.com, ORCID: 0009-0009-4161-3907

1. Introduction

The development of global urbanization has led to an increasing demand for building cementitious materials. Nowadays, Portland cement (PC) is still the most frequently used main cementitious material in the concrete industry [1–3]. However, PC has also been widely criticized for its high carbon emissions and energy consumption [4]. The grinding and calcination of cement clinker in the production process require a large amount of energy consumption, and its carbon dioxide emissions account for 8–10% of global anthropogenic carbon emissions, which cannot be underestimated [5–9]. Therefore, many researchers have been trying to find solutions to reduce PC carbon emissions, mainly including the use of cleaner energy and the use of supplementary cementitious materials to partially replace PC and reduce its use.

As a new generation of green cementitious materials, i.e., alkali-activated materials (AAM), it is considered one of the best substitutes for PC due to its complete absence of PC use and excellent performance [10–15]. Alkali-activated materials mainly use silicate or aluminosilicate industrial waste materials (mainly fly ash and ground granulated blast furnace slag) and calcined mineral kaolinite (including metakaolin) as raw materials, and can undergo hydration reaction after being activated in the presence of alkali [16–20]. Its biggest advantage is that it can achieve the recycling and utilization of industrial waste. Alkali-activated slag (AAS) also have the advantages of fast hardening, high strength, and low manufacturing cost and energy consumption. Therefore, the research and promotion of AAS have profound significance for the construction field [21].

Although alkali-activated materials have many advantages mentioned above, further exploration is still needed regarding their rheological properties and durability. Previous research has shown that many alkali-activated materials exhibit poor workability after fully mixing due to their high viscosity of paste and fast setting [22–25]. At the same time, most chemical admixtures used for PCs, such as polycarboxylate superplasticizers, exhibit lower water reducing and lubrication efficiency in AAM [26]. In addition, the autogenous shrinkage of AAS system is more severe [27]. Autogenous shrinkage refers to the gradual reduction of internal moisture due to hydration, while maintaining consistency in the external environment, resulting in negative pressure and final volume shrinkage of pores [28–31]. Research generally believes that the autogenous shrinkage of cement is highly correlated with the internal humidity of the pores and the hydration reaction process of cement paste [32, 33]. In addition, how to improve the resistance to chloride ion penetration of AAS is also an important issue that needs to be addressed in its further application in large-scale concrete engineering.

Traditional alkali-activated materials are composed of a solution mixed with an activator and water and a solid aluminosilicate precursor, thus involving the solid-liquid mixing process. However, the mixing process becomes more dangerous due to the presence of high concentrations of strong alkali, and it may corrode human skin and pose a threat to human life and health if not handled properly. As an alternative solution, the one-part alkali-activated material effectively solves this problem because its activator exists in solid form [17, 24, 26]. Therefore, only two dry powders are needed to be mixed with water to

obtain the corresponding material. Na_2CO_3 is a typical activator used for single component AAM, because its alkalinity is lower than NaOH and it has higher safety when mixed with powder precursor materials. However, the shrinkage of Na_2CO_3 activated AAS is relatively high, which will have a negative impact on the durability of the hardened samples. The incorporation of CaO to the system may not only improve volume stability, but also promote the generation of C-S-H, thereby increasing hardened strength.

Based on the above background, this study analyzed the performance of $CaO–Na_2CO_3$ activated GGBFS, including workability (flowability and rheological properties), mechanical properties, shrinkage properties, and chloride ion permeability. Furthermore, the mechanism of its performance changes was explored through isothermal calorimetry and thermogravimetric analysis. This study provides experimental and theoretical basis for the further large-scale application of $CaO–Na_2CO_3$ activated GGBFS through in-depth analysis of its performance, and is of great significance for the sustainable development of building materials.

2. Materials and experimental programs

2.1. Materials and sample preparation

The Ground Granulated Blast Furnace Slag (GGBFS) used in this study is from a mineral product processing plant in Shijiazhuang, Hebei, with a grade of S95 and a gray white color. Its particle size distribution and chemical composition are shown in Fig. 1 and Table 1, respectively. The four mix proportions used in this study are shown in Table 2. The slag content of all samples is 100 wt.%. The reactive CaO and Na_2CO_3 provided by Jalmek were chosen as alkaline activators. In these four samples, the mass fractions of CaO and Na_2CO_3 were changed to analyze their impact on the performance of AAS pastes.
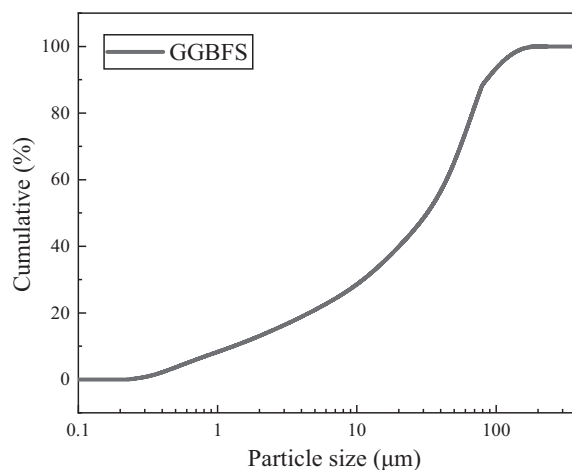

Fig. 1. Particle size distribution of GGBFS

Table 1. Chemical compositions of GGBFS

Materials	CaO	SiO$_2$	Al$_2$O$_3$	Fe$_2$O$_3$	MgO	SO$_3$	TiO$_2$	K$_2$O
GGBFS	41.6	31.8	9.87	0.72	8.10	3.19	1.58	1.02

Table 2. Mix proportion of alkali-activated GGBFS pastes

No.	Sample No.	GGBFS (wt. %)	CaO (wt. %)	Na$_2$CO$_3$ (wt. %)	w/b
1	C2N2	100	2	2	0.32
2	C2N4	100	2	4	0.32
3	C4N2	100	4	2	0.32
4	C4N4	100	4	4	0.32

2.2. Testing methods

2.2.1. Flowability

The flowability of AAS pastes were tested using a mini-cone slump mold. The upper diameter of the mold was 36 mm and the lower diameter was 60 mm, and the height was 60 mm. The mold was first placed at the center of the table, and the surface of the table and the inner wall of the cone was wetted by a damp cloth to ensure that the paste flow naturally without being affected by its adhesion to the inner wall. Subsequently, the mold was lifted vertically to allow the paste to flow to a standstill under its own gravity, and the average of its two diameters in the vertical direction was recorded. Each group of mix proportions was tested at the fresh mixing time and after resting for 60 min and 120 min. Each test was repeated three times and the average value was taken as the final flowability.

2.2.2. Rheology

The Brookfield DV3T rheometer was used for the rheological test of the AAS system, and the scheme of shear rate is shown in Fig. 2. Before conducting formal test, a 100 s^{-1} pre-shearing was applied to all pastes to achieve the same shear state. Subsequently, the shear rate was increased in the form of steps, rising from 20 s^{-1} to 100 s^{-1}. And then the shear rate was decreasing in the same way to 0 s^{-1}. Each step shear rate remained constant and lasted for 10 s. The thixotropy of fresh cement paste was calculated using the envelope area of the upper and lower curves. In addition, the descent curve was taken as the basis for calculating yield stress and plastic viscosity, and the Bingham model was used for fitting calculation, which was shown in Eq. (2.1):

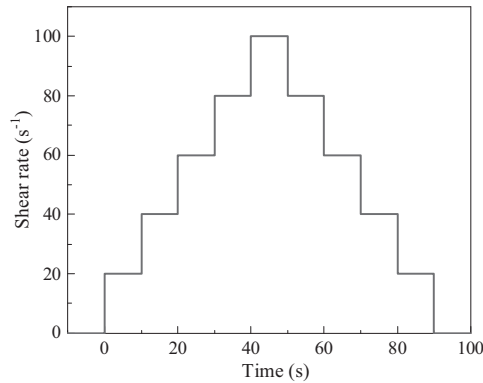$$\tau = \tau_0 + \eta\dot{\gamma}$$

(2.1)

Fig. 2. Test method of rheology

2.2.3. Compressive strength

The instrument used for testing is the DYE-300 universal press. All specimen sizes were $40 \times 40 \times 40$ mm. Firstly, the mass of precursor (GGBFS), activator, and water were weighed according to the mix proportions shown in Table 2. Then the activator was dissolved in water 24 hours in advance to eliminate the possible impact of dissolution heat on the experimental results. The GGBFS was first poured into a mixing pot and then the aqueous solution containing an activator was slowly added. The mixing procedure was to slowly mix for 150 s (62 rpm), then rest for 10 s and quickly mix for 150 s (125 rpm) until a uniform paste was obtained. The curing condition was to first cure the specimen with a mold for 24 h, during which time the upper surface of the specimen was sealed with a film to prevent moisture evaporation. Then the samples were demolded and moved to the chamber (95% RH and 20°C) to complete the remaining curing, with a duration of 3 days, 7 days, and 28 days, respectively.

2.2.4. Autogenous shrinkage

The autogenous shrinkage test was conducted using a equipment consisting of a corrugated pipe mold and a circular straight steel cylinder mold. The inner diameter of the corrugated pipe was 20 mm, and the length could be adjusted within a certain range (340 ± 5 mm) according to the test piece. The two ends of the test piece are sealed tightly. An AEC-5509 eddy current displacement sensor was used to monitor the autogenous shrinkage.

2.2.5. Chloride ion flux test

The electrical flux used in this study was based on the Chinese national standard GBT 50082-2009. The electrical flux test was conducted using specimens with a diameter of 100 mm and a height of 50 mm. After 28 days of curing, the surface of the sample was wiped dry with a cloth, sealed with epoxy resin around it, and then placed in a vacuum saturation machine for saturation treatment. Subsequently, the sample was taken out and wiped off excess moisture, and a screw was used to clamp the two test slots and the test

piece with the vulcanized rubber pad installed. A NaCl solution with a mass concentration of 3% and a NaOH solution with a molar concentration of 0.3 mol/L were injected into both sides of the tank, respectively, as shown in Fig. 3. After the solution was filled with the test tank, the power supply was connected and a constant voltage of 60 V DC was applied to record the initial current. Afterwards, the current at regular intervals for a total measurement time of 6 hours was recorded. The total electrical flux of the test piece can be calculated according to Eq. (2.2):

(2.2)
$$Q = 900 \left(I_0 + 2I_5 + 2I_{10} + \ldots + I_{360} \right)$$

where Q is the total electrical flux, I_0 is the initial current, I_5, I_{10}, $\ldots$, I_{360} is the current at the corresponding test time.
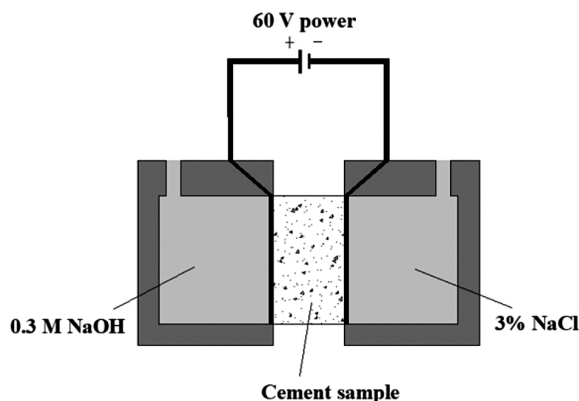
Fig. 3. Schematic diagram of chloride ion electric flux test of alkali-activated system

2.2.6. Isothermal calorimetry

The hydration heat release test of AAS in this study was conducted using a TAM Air isothermal calorimeter, and the test temperatures of the samples were all 20°. Except for powder materials, the alkali solution was placed in the instrument in advance before testing to ensure it was also at 20°. About 4 g of powder sample was taken and mixed with alkali solution according to the mix ratio, and the testing time was 72 hours.

2.2.7. Thermogravimetric analysis

The Netzsch STA 409 PC thermal analyzer was used to perform thermalgravimetric (TG) and derivative thermalgravimetric (DTG) tests on the AAS paste. The temperature was elevated from 30°C to 1000°C at a rate of 10°C/min in a nitrogen flow environment.

2.2.8. Scanning electron microscopy

The Quanta200 scanning electron microscope provided by FEI was used for morphology analysis, with a resolution of 4.0 nm and a voltage of 30 kV.

3. Results and discussion

3.1. Flowability

Figure 4 shows the flowability of alkali-activated GGBFS using CaO and Na$_2$CO$_3$ as activators. For the same mix ratio, the flow diameter was tested before and after dropping for 25 times. As shown in Fig. 4, jumping table vibration will significantly increase the flow diameter of the paste. In addition, sample with the least activator (C2N2) exhibits the highest flowability diameter both before and after vibration. As the content of CaO and Na$_2$CO$_3$ increases, the diameter after vibration decreases. Compared to C2N4, C4N2 with more CaO has a smaller flow diameter, indicating that the addition of these two solid activators reduces the early fluidity of the system.
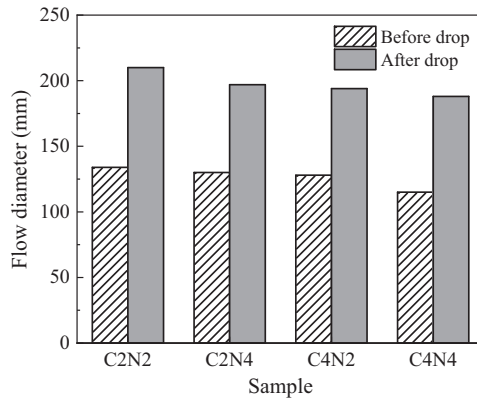
Fig. 4. Flow diameters of CaO-Na$_2$CO$_3$ activated GGBFS pastes

3.2. Rheology

Figure 5 illustrates the variation curve of shear stress with shear rate for CaO–Na$_2$CO$_3$ activated GGBFS pastes under different mix ratios. This curve can be used to calculate the yield stress and plastic viscosity of the pastes through the downward curve, and the thixotropy can also be calculated through the envelope area of the upward and downward curves. As shown in Fig. 5, C2N2 exhibits the lowest shear stress at the same shear rate. In order to better quantify the rheological and thixotropic properties of the four groups of pastes, Figs. 6 and 7 respectively show the yield stress, plastic viscosity, and thixotropic loop area calculated based on the results of Fig. 5. Similar to the previous flowability results, the plastic viscosity of C2N2 showed the lowest performance among the four groups, only 1.05 Pa•s. With the increase of activator content (including CaO and Na$_2$CO$_3$), two rheological parameters, especially yield stress, will significantly increase. When the content of CaO and Na$_2$CO$_3$ reaches 4%, the yield stress of the slurry is 61.4 Pa. Higher yield stress can make the slurry suitable for certain specific engineering applications such as 3D printing.
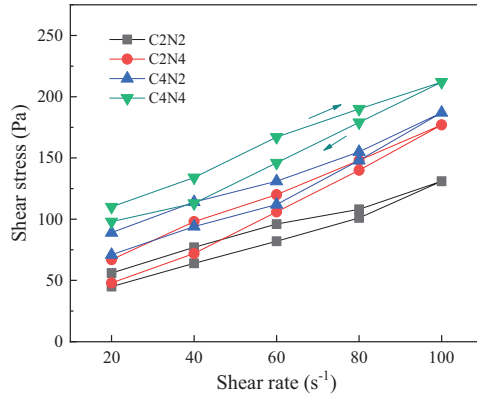
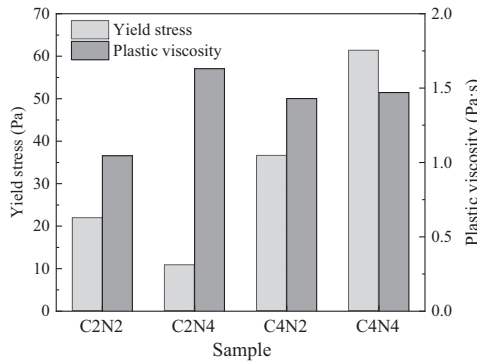Fig. 5. Rheological curves of CaO–Na$_2$CO$_3$ activated GGBFS pastes

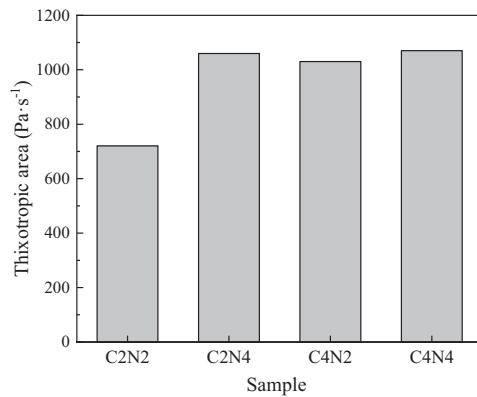Fig. 6. Yield stress and plastic viscosity of CaO–Na$_2$CO$_3$ activated GGBFS pastes

Fig. 7. Thixotropic loop area of CaO–Na$_2$CO$_3$ activated GGBFS pastes

3.3. Compressive strength

Figure 8 shows the compressive strength of four groups of alkali-activated GGBFS at 3, 7, and 28 days. As shown in Fig. 8, with the extension of curing time, the compressive strength of each group of samples significantly improved. Under the same curing time, the increase in CaO and Na$_2$CO$_3$ content to some extent improves the compressive strength. The paste containing 4% CaO and Na$_2$CO$_3$, i.e., C4N4, showed significantly higher early strength (24.3 MPa at 3 days) and later strength (40.6 MPa at 28 days) compared to the other three groups. In other words, the compressive strength of C4N4 slurry with only 2% CaO and Na$_2$CO$_3$ content was 38.8%, 21.7%, and 22.6% higher at 3, 7, and 28 days, respectively, indicating that this may be the best activated condition to date. The two solid activators selected in this study have been shown to have a significant promoting effect on the development of the mechanical properties of the samples.
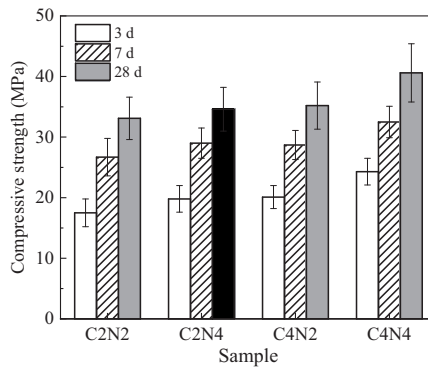

Fig. 8. Compressive strengths of CaO–Na$_2$CO$_3$ activated GGBFS pastes

3.4. Autogenous shrinkage

The development of autogenous shrinkage of AAS paste containing different CaO and Na$_2$CO$_3$ over time is shown in Fig. 9. In order to better compare the shrinkage development trend of AAS with different activator ratios, shrinkage strain was used to characterize the degree of shrinkage of the sample at a specified age. As shown in the figure, the shrinkage strain of each group of pastes gradually increases with time. However, the growth rate of contraction strain developed rapidly in the first 7 days, but gradually decreased and eventually stabilized within 7 days to 28 days. This is mainly due to the significant decrease in relative humidity inside the AAS sample. Comparing the four shrinkage curves in Fig. 9, it can be seen that the C2N2 group has the smallest shrinkage, and as the activator content increases, the shrinkage of the specimen becomes more and more severe. The data results in Fig. 9 indicate that the shrinkage values of the four groups of samples after 28 days of curing are 1230 με, 1423 με, 1394 με and 1501 με. Due to the fact that the autogenous shrinkage of alkali activated slag mainly comes from its drying shrinkage, and the evaporation of water is the main cause of drying shrinkage. The addition of activators exacerbates the shrinkage

of the system, indicating that in terms of volume stability, it is necessary to reasonably control the content of activators in order to alleviate the autogenous shrinkage of hardened samples [34–36].
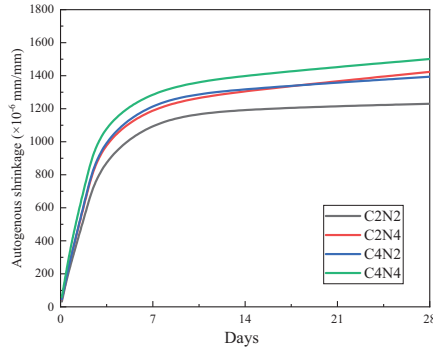

Fig. 9. Autogenous shrinkage strain of alkali-activated slag-silica fume mortars with different mix proportions

3.5. Chloride ion flux

The resistance to chloride ion penetration of concrete is an important indicator for evaluating its durability. Fig. 10 shows the total charge through the paste sample calculated by integrating the current time curve based on Eq. (2.2). It can be found that the highest electrical flux of C2N2 with the least amount of activator is 1124 C, while the increase in solid activator content leads to a decrease in this electrical flux value. This indicates that CaO and Na_2CO_3, two types of activators, improve the internal microstructure evolution of the paste and densify the hydrated sample, exhibiting better impermeability from a macro perspective. Although the difference is not significant, it can be observed from the data in Fig. 10 that the sample containing 4% CaO has lower electrical flux compared to the sample containing 4% Na_2CO_3 (987 C vs. 962 C). It indicates that CaO among the two activators has a more significant improvement in the impermeability of the sample.
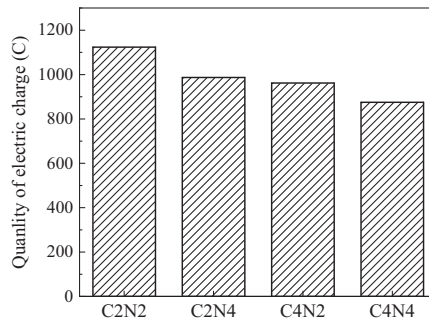

Fig. 10. Total chloride ion flux of CaO–Na_2CO_3 activated GGBFS pastes with different mix proportions

3.6. Isothermal calorimetry

The curves of hydration heat release and heat release over time of AAS pastes within 48 hours are shown in Fig. 11. The hydration mechanism of AAS system is complex, and its main product is still C–(A)–S–H gel, which is similar to PC system. However, the Ca/Si of the alkali-activated system is relatively low, and other products are related to factors such as the chemical composition of slag and other admixtures, the type and concentration of the activator, and pH value [23]. From Fig. 11, it can be seen that the hydration reaction of the AAS system is very intense in the early stage (within 4-5 hours of hydration), which is reflected in a rapid increase in the total amount of heat released. Afterwards, the hydration heat release rate of the paste significantly decreased and entered a induction period, manifested as a decrease in the total heat release growth rate. At approximately 6–8 hours, the hydration rate accelerates again and reaches its peak at 12 hours. Subsequently, the growth rate of the total heat release begins to decrease until the heat release gradually stabilizes. The highest total hydration heat release ratio in Fig. 11 within 48 hours is C4N4, with a heat release rate of 183.08 J/g. The cumulative heat release of C4N4 is significantly higher than the other three samples show that C4N4 paste has the fastest microstructural development, which may contribute to its strength development.
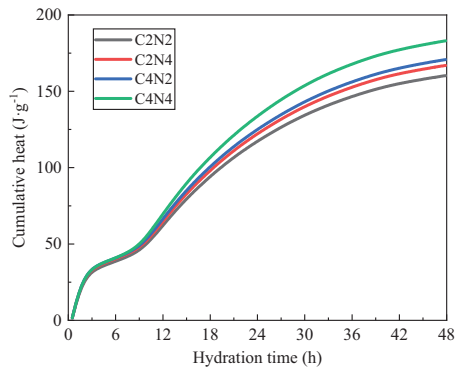

Fig. 11. Isothermal calorimetry results of CaO–Na$_2$CO$_3$ activated GGBFS pastes within 48 h of hydration

3.7. TG

Figure 12 shows the thermogravimetric analysis results of CaO–Na$_2$CO$_3$ activated GGBFS pastes. It can be seen from the figure that in the temperature range of 50–200°C, the weight loss of each group of paste is increasing, which is caused by the decomposition of C–(A)–S–H gel [12]. The maximum descent slope of the weightlessness curve is around 150–200°C. According to a previous study, the decomposition of hydrotalcite like phases occurs within the range of 250–300°C [37]. Between 600°C and 700°C, the mass loss of the phase is attributed to the CaCO$_3$ decomposition generated by the interaction between CaO and Na$_2$CO$_3$ during the reaction process [38]. From this, it can be concluded that the

introduction of CaO and Na_2CO_3 promotes the generation of C–(A)–S–H and hydrotalcite like phases, accelerates the early microstructure evolution of the paste, and thus promotes the development of strength.
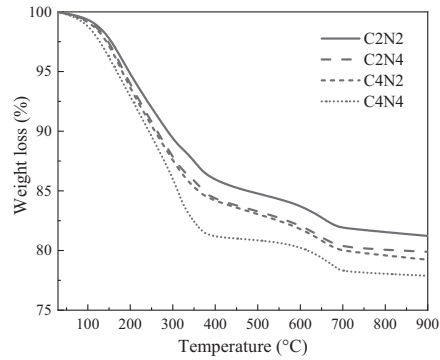

Fig. 12. TG results of CaO–Na_2CO_3 activated GGBFS pastes after 28 days of curing

3.8. SEM

Figure 13 shows the microstructure of the paste under four different mix ratios after 28 days of curing. It can be found that although there are differences in the dosage of solid activators contained in the paste, the overall overlap between hydration products is relatively
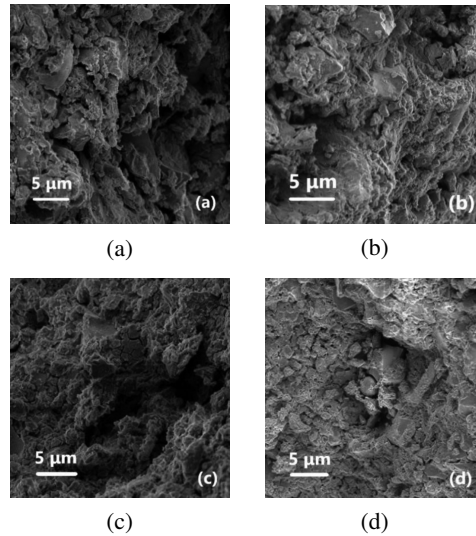
Fig. 13. SEM micrographs of CaO–Na_2CO_3 activated GGBFS pastes after 28 days of curing showing (a) C2N2, (b) C2N4, (c) C4N2, (d) C4N4

dense, which indirectly proves that it has a certain strength. The alkaline activation of CaO leads to its unique connection characteristics, which are reflected in the connection of some unreacted GGBFS particles. Due to the incomplete binding of CaO in the reaction products, some $CaCO_3$ particles were also found in the hydration products.

4. Conclusions

This study characterized the performance of AAS pastes under the combined action of CaO and Na_2CO_3 through a series of testing methods, including flowability, rheological properties, compressive strength, and durability tests. In addition, several microscopic analysis methods, including isothermal calorimetry, TG, and SEM, were used to analyze the potential mechanisms of AAS performance changes, and the following conclusions can be drawn:

1. When the water-to-binder ratio of the sample is 0.32, the flow diameter of fresh cement paste is low. The results of rheological measurement indicate that the yield stress and plastic viscosity of the paste increase with the increase of CaO and Na_2CO_3 content. The sample incorporating 4% CaO and 4% Na_2CO_3 have the highest yield stress and plastic viscosity, which are 61.4 Pa and 1.47 Pa•s, respectively.

2. The paste containing 4% CaO and Na_2CO_3, namely C4N4, showed significantly higher early strength (24.3 MPa at 3 days) and later strength (40.6 MPa at 28 days) compared to the other three groups. Furthermore, under the same content of activator, CaO has a better activation effect and a more significant promoting effect on later strength.

3. For the four groups of pastes in this study, the growth rate of shrinkage strain rapidly developed in the first 7 days, but gradually decreased and eventually stabilized after 7 days. As the content of the activator increases, the shrinkage of the specimen becomes more and more severe, with the shrinkage of C4N4 sample reaching 1501 με after 28 days of curing. However, an increase in the content of the activator results in a decrease in the electrical flux of the sample.

4. The AAS system containing CaO and Na_2CO_3 has a faster reaction rate within 4–5 hours of hydration, which is reflected in a rapid increase in hydration heat release. The increase in activator content makes the early hydration reaction more intense. The results of TG and SEM indicate that the addition of CaO and Na_2CO_3 promotes the formation of C–(A)–S–H and hydrotalcite like phases, and makes the microstructure formed after hardening of the sample denser, resulting in higher mechanical properties.

Acknowledgements

References

[1] M. Schneider, M. Romer, M. Tschudin, and H. Bolio, "Sustainable cement production—present and future", *Cement and Concrete Research*, vol. 41, no. 7, pp. 642–650, 2011, doi: 10.1016/j.cemconres.2011.03.019.

[2] F.N. Stafford, A.C. Dias, L. Arroja, J.A. Labrincha, and D. Hotza, "Life cycle assessment of the production of Portland cement: a Southern Europe case study", *Journal of Cleaner Production*, vol. 126, pp. 159–165, 2016, doi: 10.1016/j.jclepro.2016.02.110.

[3] J. Gołaszewski and M. Gołaszewska, "Properties of mortars with Calcium Sulfoaluminate cements with the addition of Portland cement and limestone", *Archives of Civil Engineering*, vol. 67, no. 2, pp. 425–435, 2021, doi: 10.24425/ace.2021.137177.

[4] W. Shen, et al., "Cement industry of China: driving force, environment impact and sustainable development", *Renewable and Sustainable Energy Reviews*, vol. 75, pp. 618–628, 2017, doi: 10.1016/j.rser.2016.11.033.

[5] S. Her, T. Park, E. Zalnezhad, and S. Bae, "Synthesis and characterization of cement clinker using recycled pulverized oyster and scallop shell as limestone substitutes", *Journal of Cleaner Production*, vol. 278, 2021, doi: 10.1016/j.jclepro.2020.123987.

[6] L. Poudyal and K. Adhikari, "Environmental sustainability in cement industry: An integrated approach for green and economical cement production", *Resources, Environment and Sustainability*, vol. 4, art. no. 100024, 2021, doi: 10.1016/j.resenv.2021.100024.

[7] W. Shen, L. Cao, Q. Li, W. Zhang, G. Wang, and C. Li, "Quantifying CO2 emissions from China's cement industry", *Renewable and Sustainable Energy Reviews*, vol. 50, pp. 1004–1012, 2015, doi: 10.1016/j.rser.2015.05.031.

[8] K. Kuzmenko, N. Ducoulombier, A. Feraille, and N. Roussel, "Environmental impact of extrusion-based additive manufacturing: generic model, power measurements and influence of printing resolution", *Cement and Concrete Research*, vol. 157, art. no. 106807, 2022, doi: 10.1016/j.cemconres.2022.106807.

[9] R.M. Andrew, "Global CO 2 emissions from cement production", *Earth System Science Data*, vol. 10, no. 1, pp. 195–217, 2018.

[10] A. Palomo, M. Grutzeck, and M. Blanco, "Alkali-activated fly ashes: A cement for the future", *Cement and Concrete Research*, vol. 29, no. 8, pp. 1323–1329, 1999, doi: 10.1016/S0008-8846(98)00243-9.

[11] F. Puertas, S. Martìinez-Ramìrez, S. Alonso, and T. Vazquez, "Alkali-activated fly ash/slag cements: strength behaviour and hydration products", *Cement and Concrete Research*, vol. 30, no. 10, pp. 1625–1632, 2000, doi: 10.1016/S0008-8846(00)00298-2.

[12] M.B. Haha, G. Le Saout, F. Winnefeld, and B. Lothenbach, "Influence of activator type on hydration kinetics, hydrate assemblage and microstructural development of alkali activated blast-furnace slags", *Cement and Concrete Research*, vol. 41, no. 3, pp. 301–310, 2011, doi: 10.1016/j.cemconres.2010.11.016.

[13] F. Pacheco-Torgal, Z. Abdollahnejad, A. Camões, M. Jamshidi, and Y. Ding, "Durability of alkali-activated binders: a clear advantage over Portland cement or an unproven issue?", *Construction and Building Materials*, vol. 30, pp. 400–405, 2012, doi: 10.1016/j.conbuildmat.2011.12.017.

[14] J.L. Provis, "Alkali-activated materials", *Cement and Concrete Research*, vol. 114, pp. 40–48, 2018, doi: 10.1016/j.cemconres.2017.02.009.

[15] C. Lu, Z. Zhang, C. Shi, N. Li, D. Jiao, and Q. Yuan, "Rheology of alkali-activated materials: A review", *Cement and Concrete Composites*, vol. 121, art. no. 104061, 2021, doi: 10.1016/j.cemconcomp.2021.104061.

[16] A. Poulesquen, F. Frizon, and D. Lambertin, "Rheological behavior of alkali-activated metakaolin during geopolymerization", *Journal of Non-Crystalline Solids*, vol. 357, no. 21, pp. 3565–3571, 2011, doi: 10.1016/j.jnoncrysol.2011.07.013.

[17] T. Luukkonen, Z. Abdollahnejad, J. Yliniemi, P. Kinnunen, and M. Illikainen, "One-part alkali-activated materials: A review", *Cement and Concrete Research*, vol. 103, pp. 21–34, 2018, doi: 10.1016/j.cemconres.2017.10.001.

[18] A. Wang, et al., "The durability of alkali-activated materials in comparison with ordinary Portland cements and concretes: a review", *Engineering*, vol. 6, no. 6, pp. 695–706, 2020, doi: 10.1016/j.eng.2019.08.019.

[19] M. Komljenović, Z. Baščarević, and V. Bradić, "Mechanical and microstructural properties of alkali-activated fly ash geopolymers", *Journal of Hazardous Materials*, vol. 181, no. 1-3, pp. 35–42, 2010, doi: 10.1016/j.jhazmat.2010.04.064.

[20] M.O. Yusuf, M.A.M. Johari, Z.A. Ahmad, and M. Maslehuddin, "Strength and microstructure of alkali-activated binary blended binder containing palm oil fuel ash and ground blast-furnace slag", *Construction and Building Materials*, vol. 52, pp. 504–510, 2014, doi: 10.1016/j.conbuildmat.2013.11.012.

[21] N. Li, N. Farzadnia, and C. Shi, "Microstructural changes in alkali-activated slag mortars induced by accelerated carbonation", *Cement and Concrete Research*, vol. 100, pp. 214–226, 2017, doi: 10.1016/j.cemconres.2017.07.008.

[22] T. Yang, H. Zhu, Z. Zhang, X. Gao, C. Zhang, and Q. Wu, "Effect of fly ash microsphere on the rheology and microstructure of alkali-activated fly ash/slag pastes", *Cement and Concrete Research*, vol. 109, pp. 198–207, 2018, doi: 10.1016/j.cemconres.2018.04.008.

[23] H. Alghamdi, S.A.O. Nair, and N. Neithalath, "Insights into material design, extrusion rheology, and properties of 3D-printable alkali-activated fly ash-based binders", *Materials & Design*, vol. 167, 2019, doi: 10.1016/j.matdes.2019.107634.

[24] L. Li, J.-X. Lu, B. Zhang, and C.-S. Poon, "Rheology behavior of one-part alkali activated slag/glass powder (AASG) pastes", *Construction and Building Materials*, vol. 258, 2020, doi: 10.1016/j.conbuildmat.2020.120381.

[25] Y. Chen, C. Liu, R. Cao, C. Chen, V. Mechtcherine, and Y. Zhang, "Systematical investigation of rheological performance regarding 3D printing process for alkali-activated materials: Effect of precursor nature", *Cement and Concrete Composites*, vol. 128, art. no. 104450, 2022, doi: 10.1016/j.cemconcomp.2022.104450.

[26] Y. Alrefaei, Y.-S. Wang, and J.-G. Dai, "The effectiveness of different superplasticizers in ambient cured one-part alkali activated pastes", *Cement and Concrete Composites*, vol. 97, pp. 166–174, 2019, doi: 10.1016/j.cemconcomp.2018.12.027.

[27] E. Adesanya, A. Aladejare, A. Adediran, A. Lawal, and M. Illikainen, "Predicting shrinkage of alkali-activated blast furnace-fly ash mortars using artificial neural network (ANN)", *Cement & Concrete Composites*, vol. 124, art. no. 104265, 2021, doi: 10.1016/j.cemconcomp.2021.104265.

[28] A.A.M. Neto, M.A. Cincotto, and W. Repette, "Drying and autogenous shrinkage of pastes and mortars with activated slag cement", *Cement and Concrete Research*, vol. 38, no. 4, pp. 565–574, 2008, doi: 10.1016/j.cemconres.2007.11.002.

[29] A. Domingo-Cabo, C. Lázaro, F. López-Gayarre, M. Serrano-López, P. Serna, and J. O. Castaño-Tabares, "Creep and shrinkage of recycled aggregate concrete", *Construction and Building Materials*, vol. 23, no. 7, pp. 2545–2553, 2009, doi: 10.1016/j.conbuildmat.2009.02.018.

[30] A. Gonzalez-Corominas and M. Etxeberria, "Effects of using recycled concrete aggregates on the shrinkage of high performance concrete", *Construction and Building Materials*, vol. 115, pp. 32–41, 2016, doi: 10.1016/j.conbuildmat.2016.04.031.

[31] G.M. Moelich, J. Kruger, and R. Combrinck, "Plastic shrinkage cracking in 3D printed concrete", *Composites Part B: Engineering*, vol. 200, art. no. 108313, 2020, doi: 10.1016/j.compositesb.2020.108313.

[32] S. Yang, "Effect of different types of recycled concrete aggregates on equivalent concrete strength and drying shrinkage properties", *Applied Sciences*, vol. 8, no. 11, art. no. 2190, 2018, doi: 10.3390/app8112190.

[33] J. Xiang, L. Liu, X. Cui, Y. He, G. Zheng, and C. Shi, "Effect of Fuller-fine sand on rheological, drying shrinkage, and microstructural properties of metakaolin-based geopolymer grouting materials", *Cement and Concrete Composites*, vol. 104, 2019, doi: 10.1016/j.cemconcomp.2019.103381.

[34] B. Zhang, H. Zhu, Y. Cheng, G.F. Huseien, and K.W. Shah, "Shrinkage mechanisms and shrinkage-mitigating strategies of alkali-activated slag composites: A critical review", *Construction and Building Materials*, vol. 318, art. no. 125993, 2022, doi: 10.1016/j.conbuildmat.2021.125993.

[35] H. Ye and A. Radlińska, "Shrinkage mechanisms of alkali-activated slag", *Cement and Concrete Research*, vol. 88, pp. 126–135, 2016, doi: 10.1016/j.cemconres.2016.07.001.

[36] H. Ye and A. Radlińska, "Shrinkage mitigation strategies in alkali-activated slag", *Cement and Concrete Research*, vol. 101, pp. 131–143, 2017, doi: 10.1016/j.cemconres.2017.08.025.

[37] J.C. Roelofs, J.A. van Bokhoven, A.J. Van Dillen, J.W. Geus, and K.P. de Jong, "The thermal decomposition of Mg–Al hydrotalcites: effects of interlayer anions and characteristics of the final structure", *Chemistry–A European Journal*, vol. 8, no. 24, pp. 5571–5579, 2002, doi: 10.1002/1521-3765(20021216)8:24<5571::AID-CHEM5571>3.0.CO;2-R.

[38] K.S. Karunadasa, C. Manoratne, H. Pitawala, and R. Rajapakse, "Thermal decomposition of calcium carbonate (calcite polymorph) as examined by in-situ high-temperature X-ray powder diffraction", *Journal of Physics and Chemistry of Solids*, vol. 134, pp. 21–28, 2019, doi: 10.1016/j.jpcs.2019.05.023.